

Compact Reconnaissance Imaging Spectrometer for Mars investigation and data set from the Mars Reconnaissance Orbiter's primary science phase

Scott L. Murchie,¹ Frank P. Seelos,¹ Christopher D. Hash,² David C. Humm,¹ Erick Malaret,² J. Andrew McGovern,¹ Teck H. Choo,¹ Kimberly D. Seelos,¹ Debra L. Buczkowski,¹ M. Frank Morgan,¹ Olivier S. Barnouin-Jha,¹ Hari Nair,¹ Howard W. Taylor,¹ Gerald W. Patterson,¹ Christopher A. Harvel,¹ John F. Mustard,³ Raymond E. Arvidson,⁴ Patrick McGuire,^{4,5} Michael D. Smith,⁶ Michael J. Wolff,⁷ Timothy N. Titus,⁸ Jean-Pierre Bibring,⁹ and Francois Poulet⁹

Received 24 January 2009; revised 22 May 2009; accepted 22 June 2009; published 1 October 2009.

[1] The part of the Compact Reconnaissance Imaging Spectrometer (CRISM) for Mars investigation conducted during the Mars Reconnaissance Orbiter's (MRO's) primary science phase was a comprehensive investigation of past aqueous environments, structure of the planet's crust, past climate, and current meteorology. The measurements to implement this investigation include over 9500 targeted observations of surface features taken at spatial resolutions of better than 40 m/pixel, monitoring of seasonal variations in atmospheric aerosols and trace gases, and acquisition of a 200 m/pixel map covering over 55% of Mars in 72 selected wavelengths under conditions of relatively low atmospheric opacity. Key results from these data include recognition of a diversity of aqueous mineral-containing deposits, discovery of a widespread distribution of phyllosilicates in early to middle Noachian units, the first definitive detection of carbonates in bedrock, new constraints on the sequence of events that formed Hesperian-aged, sulfate-rich layered deposits, characterization of seasonal polar processes, and monitoring of the 2007 global dust event. Here we describe CRISM's science investigations during the Primary Science Phase, the data sets that were collected and their calibration and uncertainties, and how they have been processed and made available to the scientific community. We also describe the ongoing investigation during MRO's extended science phase.

Citation: Murchie, S. L., et al. (2009), Compact Reconnaissance Imaging Spectrometer for Mars investigation and data set from the Mars Reconnaissance Orbiter's primary science phase, *J. Geophys. Res.*, 114, E00D07, doi:10.1029/2009JE003344.

1. Introduction

[2] The Compact Reconnaissance Imaging Spectrometer for Mars (CRISM) [Murchie *et al.*, 2007a] is one of six major science instruments on the Mars Reconnaissance Orbiter (MRO), along with the High Resolution Imaging Science Experiment (HiRISE) [McEwen *et al.*, 2007], the

Mars Color Imager (MARCI), Context Imager (CTX) [Malin *et al.*, 2007], the Mars Climate Sounder (MCS) [McCleese *et al.*, 2007], and the Shallow Radar (SHARAD) [Seu *et al.*, 2007]. The three primary science objectives of the MRO mission are (1) to search for evidence of aqueous and/or hydrothermal activity; (2) to map and characterize the composition, geology, and stratigraphy of surface deposits; and (3) to characterize seasonal variations in dust and ice aerosols and water content of surface materials, recovering science lost with the failure of the Mars Climate Orbiter. MRO's two secondary objectives are (1) to provide information on the atmosphere complementary to the reflight MCO investigations, and (2) to identify new sites with high science potential for future investigation. MRO has completed its primary science phase (PSP), which lasted from November 2006 to November 2008. During that time the spacecraft operated in a sun-synchronous, near-circular (255 × 320 km altitude), near-polar orbit with a mean local solar time of 1510. The observations acquired include a variety of regional to global mapping and atmospheric

¹Johns Hopkins University Applied Physics Laboratory, Laurel, Maryland, USA.

²Applied Coherent Technology, Herndon, Virginia, USA.

³Department of Geological Sciences, Brown University, Providence, Rhode Island, USA.

⁴Department of Earth and Planetary Sciences, Washington University, Saint Louis, Missouri, USA.

⁵Freie Universität, Berlin, Germany.

⁶NASA Goddard Space Flight Center, Greenbelt, Maryland, USA.

⁷Space Science Institute, Boulder, Colorado, USA.

⁸U.S. Geological Survey, Flagstaff, Arizona, USA.

⁹Institut d'Astrophysique Spatiale, Université Paris Sud, Orsay, France.

monitoring campaigns, plus a series of targeted observations in which the spacecraft actively pointed the coboresighted HiRISE, CRISM, and CTX instruments to measure a series of geologic targets at high spatial resolution. The mission's objectives, design, and implementation were summarized by Zurek and Smrekar [2007].

[3] In this paper we briefly review the specific objectives of the CRISM investigation during the PSP, the measurement strategies used to address them, and the key results. We summarize the data sets acquired during the PSP, and how they have been calibrated, processed, and made available to the scientific community. We also summarize observational and data product generation plans for MRO's second Mars year of operations, the extended science phase (ESP).

2. Instrument Operation Overview

[4] The CRISM instrument and its operating modes used during data acquisition were described in detail by Murchie *et al.* [2007a, 2007b]. The following summary provides background for how the instrument hardware capabilities were used in PSP measurement campaigns to address MRO's primary and secondary science objectives, and for the creation of data products from those measurements.

[5] The CRISM instrument consists of three assemblies. The largest, the Optical Sensor Unit (OSU), contains optics, detectors, radiators, and a cryogenic system, all of which can be gimballed, or pivoted, to track Mars' surface. A Data Processing Unit (DPU) provides power, command and control, and data editing and compression, and the Gimbal Motor Electronics (GME) runs the gimbal.

[6] The OSU contains telescope optics that focus light on a slit to form an image one line high and approximately 600 columns wide. After the light passes through the slit, a beam splitter directs it to two independent grating spectrometers with separate detectors. In each spectrometer, the one-line spatial image is dispersed into its component wavelengths that are reimaged onto different rows of that spectrometer's detector. One spectrometer, denoted as visible near infrared (VNIR), uses an array of silicon photodiodes to capture spatial/spectral images covering the wavelengths 362–1053 nm. The other spectrometer, denoted as infrared (IR), uses an array of HgCdTe diodes to take spatial/spectral images at 1002–3920 nm. Both spectrometers sample the spectrum at 6.55 nm per detector row. Both detectors have fixed-mounted filters with two or three wavelength zones, to block higher orders from the grating and, in the case of the IR detector, to attenuate thermal emissions from the spectrometer cavity. Each detector is also wider than the image of the scene; spare columns at the sides of the detectors do not contain scene information, but do detect wavelength-dependent, diffuse scattering of light from the grating that has to be removed during calibration. A cryogenic cooling system maintains the IR detector at -148°C to -163°C to limit noise, and the spectrometer housing is cooled by a passive radiator to -70°C to -78°C to limit thermal background. The temperature of the VNIR detector drifts with that of the spectrometer housing, and typically is -55°C to -65°C .

[7] The DPU provides power and command-and-control, and also data editing capabilities to manage data volume

and to establish operating modes for the instrument. To remove smear, an along-track gimbaling capability can be used to track a point on the surface and scan across it slowly. Frame rates of 1, 3.75, 15, and 30 Hz can also be used to manage pixel smear. Data editing capabilities include selection of which wavelength channels are down-linked, and binning of pixels in the spatial direction. The two major choices for the number of wavelengths is the 544 detector rows with useful amounts of scene radiance, or 72 rows selected for their coverage of key wavelengths that separate major mineral phases [Pelkey *et al.*, 2007]. (In each case, one extra detector row is included for calibration purposes.) Spatial binning of pixels can be done using groups of 1, 2, 5, or 10 pixels in the cross-track spectral direction. Pixels are "squared" in the along-track direction by adjusting frame rate and/or the rate of gimbal motion.

[8] CRISM's two basic operating modes are targeted, in which the gimbal is used for image motion compensation, and fixed pointing at spacecraft nadir. In targeted observations the gimbal is scanned to track a point on the surface and prevent smear from motion of the spacecraft. A super-imposed scan slowly sweeps the field of view across a region approximately $10\text{ km} \times 10\text{ km}$ over 2–3 min to acquire an unsmeared image of a target area. For geologic targets, surrounding the time of closest approach, 350 to 540 image lines are acquired at a frame rate of 3.75 Hz. Spatial sampling is 18 m/pixel using no spatial pixel binning, or 36 m/pixel for $2\times$ binning. Ten to twelve additional abbreviated, $10\times$ spatially binned images are taken before and after the main image, providing measurements of the same scene with different path lengths through the atmosphere. This sequence of multiple measurements at different geometries is called an emission phase function, or EPF. When analyzed using a radiative transfer model that incorporates a model of surface scattering and wavelength-dependent attenuation by atmospheric gases and aerosols, an EPF allows separation of atmospheric and surface radiances. For investigation of the atmosphere, the central image can also be $10\times$ binned to minimize data volume. All targeted measurements are taken in 544 wavelength channels covering 0.36–3.92 microns with 6.55 nm spectral sampling. The 11 to 13 spatial images taken during the gimbal's tracking of a target constitute a single, multiimage observation.

[9] CRISM can also build up images using passive, fixed pointing, and this is done in either of two ways. First, images are acquired at 15 Hz with $10\times$ spatial pixel binning, or 30 Hz with $5\times$ spatial pixel binning, yielding pixel footprints of 200 or 100 m, respectively. When it operates in this mode, CRISM returns data from only 72 wavelengths. The 200 m/pixel mode is used almost exclusively to map Mars globally, or to "ride-along" with MRO's other cameras when the available data volume or a crowded observing schedule limits the number of targeted observations. Second, data can be taken at a lower frame rate of 3.75 Hz using $10\times$ spatial pixel binning and all 544 wavelengths. The mode of operation measures a $10 \times 10\text{ km}$ spot hyperspectrally with minimal data volume and is used to monitor atmospheric gases.

[10] Internal instrument calibrations are taken interleaved with and as part of all observations. An internal shutter is closed to take dark measurements (of IR background due to emission inside the instrument) every 3 min. One or more

Table 1. Mapping of MRO Objectives to Derived CRISM Science Objectives, Measurement Strategies, and Key Findings From the PSP^a

MRO Science Objective	CRISM Science Objective	Relevant CRISM Measurements	Key Findings
Search for evidence of aqueous and/or hydrothermal activity	Identify and map mineral deposits indicating the characteristics and distributions of past water environments	Multispectral survey mapping to inventory the distribution and geologic settings of aqueous deposits. High spatial and spectral targeted observations to characterize selected sites in detail, coordinated with HiRISE and CTX imaging.	At least 10 distinct classes of deposits with different morphologies, geologic settings, and ages contain concentrations of aqueous minerals. ^b Major classes of alteration products include phyllosilicates, carbonates, hydrated silica, and sulfates. ^{b,c,d,e,f,g,h}
Map and characterize the composition, geology, and stratigraphy of surface deposits	Map the distribution of mineral phases indicative igneous and sedimentary rock units	Multispectral survey mapping to provide context. High spatial and spectral targeted observations to characterize selected sites in detail, coordinated with HiRISE and CTX imaging.	Noachian crust contains a complex stratigraphy of volcanic materials of different composition with phyllosilicate and carbonate-bearing materials. ^{b,c,d,e,j,n,o} This is superposed by Hesperian-aged volcanics, and hydrated silica- and sulfate-containing deposits. ^{f,g,h,i,j,p}
Characterize seasonal variations in dust and ice aerosols and water content of surface materials	Monitor spatial and seasonal variation in trace gases and aerosols. Monitor formation and ablation of H ₂ O and CO ₂ ices in the seasonal cap	Regular emission phase functions, in repeating latitude/longitude grid. Nadir hyperspectral measurements to fill time between targeted observations and multispectral survey. Regular monitoring of volatile condensation and sublimation at selected circumpolar sites, coordinated with HiRISE and CTX imaging.	Spatial and seasonal variations in CO, H ₂ O vapor, O ₃ , and dust and ice aerosols. ^k 2007 global dust event was monitored, and more accurate scattering properties of dust determined. ^l Monitoring of selected polar sites revealed processes of H ₂ O and CO ₂ condensation and sublimation. ^m
Provide information on the atmosphere complementary to reflow MCO investigations	Measure record of Mars' early climate recorded as mineral deposits	High spectral resolution targeted measurements to identify minerals diagnostic of past environments and search for carbonates.	A regional occurrence of carbonate rocks traps CO ₂ , but not enough for an early, thick atmosphere. ^e A diversity of hydrated silicate and sulfates phases records past temporal and spatial variations in the near-surface environment. ^{b,c,d,e,f,g,h,i,j}
Identify new sites with high science potential for future investigation	Identify previously undiscovered sites with a mineral record of past water environments	Multispectral survey mapping at key wavelengths to identify new mineral exposures. Follow-up high-resolution coordinated observations by CRISM, HiRISE, and CTX.	New classes of deposits discovered include carbonates, hydrated silica, mixed kaolinite/acid sulfates, phyllosilicate-rich deltaic deposits. ^{e,f,n,o,p} ~10,000 exposures >1 km ² predominantly in Noachian units. ^{b,c}

^aMRO, Mars Reconnaissance Orbiter; CRISM, Compact Reconnaissance Imaging Spectrometer; PSP, primary science phase.^bMurchie et al. [2009a].^cMustard et al. [2008].^dBishop et al. [2008].^eEhlmann et al. [2008b].^fMilliken et al. [2008].^gMurchie et al. [2009b].^hBishop et al. [2007].ⁱRoach et al. [2009].^jMcKeown et al. [2009].^kSmith et al. [2009].^lWolff et al. [2007].^mTitus et al. [2008].ⁿGrant et al. [2008].^oEhlmann et al. [2008a].^pWray et al. [2009].



Figure 1. Coverage by multispectral survey data acquired during the PSP. The data are shown here in Mollweide projection centered at 0° latitude, 0° longitude, with the 0.60-, 0.53-, and 0.44- μm wavelengths displayed in the red, green, and blue image planes.

times daily a sequence of dark images is taken at different exposure times to estimate the “bias,” or response of the IR detector to zero input photons. Also, multiple times daily, an onboard, closed-loop controlled integrating sphere is measured to provide a snapshot of the detectors’ time-variable responsivity to input radiance. During the PSP, in addition to the background measurements acquired as part of 35,735 observations of Mars’ surface and atmosphere, and additional 6523 free-standing calibration observations were obtained.

3. Science Measurement Strategy and Results Overview

3.1. Science Objectives and Corresponding Measurements

[11] As described by Murchie *et al.* [2007a], CRISM addresses all five of MRO’s primary and secondary objectives using its ability to measure absorption features diagnostic of the primary igneous minerals olivine and pyroxene, their alteration products including phyllosilicates, zeolite, sulfate, carbonate, and silica, and the atmospheric trace gases CO, H₂O, and O₃. For surface measurements, the instrument’s capability for high spatial resolution enables resolving mineralogic differences over $\sim 40\text{-m}$ scales. The mapping of MRO’s primary and secondary objectives to CRISM’s objectives, the series of measurement campaigns used to address those objectives, and key results from the PSP are summarized in Table 1.

[12] During the PSP, CRISM used three distinct measurement campaigns to address its science objectives. These are described in Table 2. The first campaign was acquisition of a global, 200 m/pixel, 72-wavelength map. This data set, known as the “multispectral survey,” shows the distribution of major crustal components at about five times the average spatial resolution of the Observatoire pour la Minéralogie, L’Eau, les Glaces et l’Activité (OMEGA) data set [Bibring *et al.*, 2005], and allows identification of previously undiscovered exposures of aqueous minerals and their follow-up investigation at high spatial resolution. The gimbal is pointed at nadir, data are collected at a frame rate

of 15 Hz, and spatial pixels are binned cross track by $10\times$ yielding a data set with ~ 200 m/pixel spatial sampling. During the PSP approximately 63% of the planet was covered using 15,855 multispectral survey observations, each consisting of one or more image strips acquired over a 3-min or shorter duration (to allow interspersing of background measurements). File names of data products generated from these observations all begin with the character string “MSP” (for “multispectral survey”). Part of these data were acquired during the 2007 global dust event. Excluding those data most affected (from the period 25 June 2007 through 29 September 2007), a total spatial coverage of just over 55% was obtained and is illustrated in Figure 1.

[13] The second measurement campaign was the atmospheric survey, whose objectives were to characterize seasonal variations in the total column abundances of atmospheric dust and ice aerosols and trace gases including CO, H₂O, and O₃, and seasonal variations in the water content of surface materials. This campaign was intended to complement daily maps of the spatial distributions of aerosols and trace gases by MCS. At the beginning of the PSP, the atmospheric survey consisted of repetitive global grids of EPFs. A dense grid was taken over about a 2-week period in six parts, every 10 weeks. In each of the six parts the along-track spacing between EPFs was about 22°, and the ground tracks were 54° of longitude apart (six or seven terminator-to-terminator sequences of EPFs were taken every other orbit for one Mars sol). The six parts, or sols, were staggered both in longitude and time to yield 11° latitude sampling and 9° longitude sampling. The exact repeat times of this pattern every 10 weeks were selected to provide repetitive coverage of surface coordinates to within ± 50 km, and SHARAD measurements were taken simultaneously to track changes in surface dielectric properties as surface water content changed. Between the 10-week repeats, two other groups of two Martian sols were similarly devoted to EPFs on every other orbit, with each group of two sols providing about 27° longitude sampling of the atmosphere. Thus, on average, a grid of EPFs sampled the atmosphere about every 5° of solar longitude (Ls), and the dense grids on 10-week repeats provides sampling every

Table 2. Descriptions of CRISM's Observation Campaigns and the Data Products Generated by Them

Observing Campaign	Gimbal Pointing and Number of Images	Observations Type and Description	Data Product Nomenclature
Targeted observations	Gimbal tracks surface with superimposed scan for each image 1 high-resolution image, 10 reduced-resolution EPF images	Full resolution targeted; Spatial pixels unbinned for target (18 m/pixel @300 km); Spatial pixels 10× binned for EPFs	FRT...
		Half resolution short targeted; Spatial pixels 2× binned for target (36 m/pixel @300 km); Spatial pixels 10× binned for EPFs	HRS...
		Half resolution long targeted; Spatial pixels 2× binned for target (36 m/pixel @300 km); 2× swath length as above; Spatial pixels 10× binned for EPFs	HRL...
Atmospheric survey	Gimbal track surface with superimposed scan for each image 11 or 13 reduced-resolution images	EPF; spatial pixels 10× binned (~200 m/pixel @300 km); 9° lon. × 11° latitude grid every ~36° of Ls; 27° lon. × 11° latitude grid every ~5° of Ls	EPF...
	Nadir-pointed; multiple images	Tracking Optical Depth; Spatial pixels 10× binned (200 × 900 m/pixel @300 km)	TOD...
Multispectral survey	Nadir-pointed; multiple images	Multispectral survey; 73 channels, spatial pixels 10× binned (~200 m/pixel @300 km)	MSP...
		Multispectral windows; 73 channels, spatial pixels 5× binned (~100 m/pixel @300 km)	MSW...

~36° of Ls. Over the course of the PSP 3828 gimbaled observations consisting solely of 10× binned EPFs were taken as part of these grids. File names of data products generated from these observations all begin with the character string “EPF” (for “emission phase function”). At times of high MRO data downlink rates, selected observations within the grids were upgraded to higher spatial resolution targeted observations.

[14] Early in the PSP, MCS suspended regular nadir measurements and focused on another of its measurement objectives, limb profiles, eliminating the high spatial and temporal frequency measurements of trace gas abundances that were initially assumed to complement EPF measure-

ments. To replace this vital complementary measurement set, a new CRISM operating mode was defined using existing instrument capabilities. Beginning at Ls 290°, short bursts of nadir-pointed measurements using all 544 wavelengths and 10 × spatial binning were acquired during times when CRISM was not acquiring other higher-priority observations, each burst sampling a 10 × 10 km region every 2° of latitude along track. These samples provide a capability to estimate column abundances of trace gases, but without an emission phase function the accuracy is less, and dust opacity cannot be uniquely retrieved. Through the end of the PSP, 3784 observations consisting of sequences of the bursts were taken. File names of data products generated

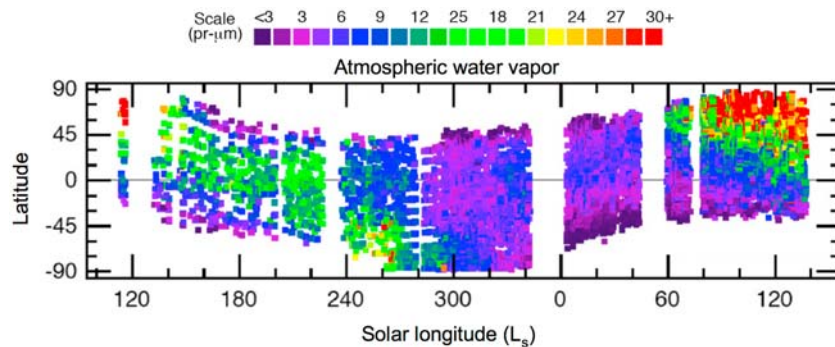


Figure 2. Coverage of Mars in latitude and Ls by CRISM's atmospheric survey acquired during the PSP. The values shown are estimated precipitable microns of atmospheric H₂O vapor, calculated from several narrow absorptions near 2.6 μm. Coarser sampling prior to Ls 290° is where only emission phase functions (EPFs) were used, and denser sampling later is when both EPFs and tracking optical depths (TODs) were used. Adapted from *Smith et al.* [2009].

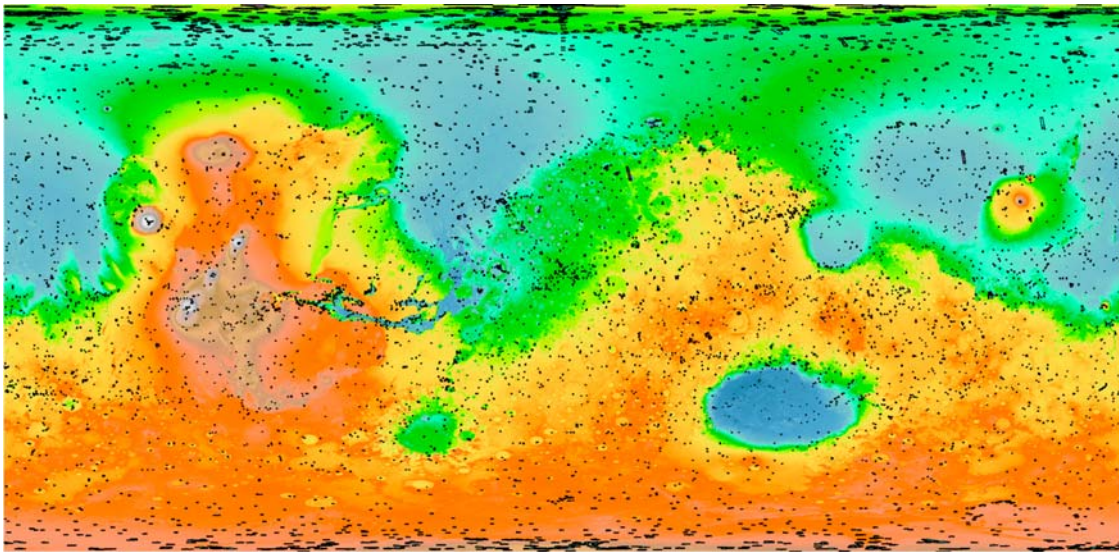


Figure 3. Coverage of Mars by CRISM targeted observations taken during the PSP, indicated by black symbols overlain on a color-coded Mars Orbiter Laser Altimeter elevation map in which redder colors indicate higher elevations. The map is in equirectangular projection centered at 0° latitude, 0° longitude.

from these observations all begin with the character string for “tracking optical depth” (TOD). Figure 2 shows the latitude and Ls distribution of atmospheric survey measurements during the PSP; the addition of TODs dramatically improved spatial and temporal sampling of trace gas variations.

[15] CRISM’s third (and its primary) measurement campaign was to identify and map the distribution of key minerals at high spatial resolution, at thousands of high-priority targets including candidate sedimentary deposits, volcanic regions, crustal sections exposed in steep escarpments, and sites which exhibit evidence for concentrations of aqueously formed minerals. This was accomplished using targeted observations with unbinned or $2\times$ binned central images. Binning was used in some cases to conserve data volume, and in other cases to allow acquisition of a longer central image (10×20 km) in the same amount of time, when areal coverage was deemed more important than spatial resolution. Typically, the observations were coordinated with HiRISE and CTX to provide simultaneous, overlapping coverage. The regions of interest selected for targeting were initially compiled from mineralogical exposures identified by OMEGA, the Thermal Emission Spectrometer (TES) on Mars Global Surveyor [Christensen *et al.*, 2001b], and the Thermal Emission Imaging System (THEMIS) on Mars Odyssey [Christensen *et al.*, 2004], formations with light-toned layering identified in images from the Mars Orbiter Camera (MOC) on Mars Global Surveyor [Malin *et al.*, 1992] and from THEMIS, and sites for polar monitoring identified from OMEGA, THEMIS, and MOC data. Later, regions of interest identified in HiRISE or CTX images and in CRISM’s multispectral survey were also targeted. File names of data products generated from targeted observations begin with the character string for “full resolution target” (FRT) if the central image is unbinned, for “half resolution short” (HRS) if it is $2\times$ binned but comparable in size, or “half resolution long” (HRL) if $2\times$ binned and extended in length along track.

During the PSP 9514 targeted observations were acquired of which 6674 were FRTs, 1905 were HRLs, and 935 were HRSs. Their locations are shown on a MOLA elevation map in Figure 3. Targeted observations are globally distributed, but concentrated in areas with previously known exposures of aqueous mineralogy including Valles Marineris, Terra Meridiani, and the regions around Mawrth Vallis and Nili Fossae.

3.2. Overview of the First Results

[16] The first analyses of multispectral survey and targeted observations have changed the paradigm for the extent and diversity of water-rock interactions on early Mars. Global mapping by TES revealed only limited evidence for altered phases, namely coarse-grained hematite associated with Hesperian-aged layered deposits in Meridiani Planum and Valles Marineris [Christensen *et al.*, 2001a], and furthermore revealed extensive outcrops of olivine that would easily have weathered in the presence of liquid water [Hoefen *et al.*, 2003; Hamilton and Christensen, 2005; Edwards *et al.*, 2008]. These findings led to a preliminary interpretation that aqueous alteration had had only an extremely limited role in formation of Mars’ crustal rocks. Later, mapping at visible to near-infrared wavelengths by OMEGA revealed dozens of outcrops of phyllosilicates in Noachian terrains, and that the layered deposits in Meridiani Planum and Valles Marineris as well as Amazonian-aged deposits in the north circumpolar dune field contain a large fraction of sulfate minerals [Bibring *et al.*, 2005; Gendrin *et al.*, 2005; Langevin *et al.*, 2005]. OMEGA’s findings suggested that aqueous alteration of the crust began earlier than thought from TES data, and progressed with time from a neutral to acidic environment [Bibring *et al.*, 2006].

[17] CRISM’s results dramatically expand the scope and diversity of known mineralogies and geologic settings of aqueous alteration products. In contrast to the dozens of phyllosilicate exposures detected in OMEGA data, CRISM’s multispectral survey reveals many thousands of

resolvable exposures in Noachian units [Mustard *et al.*, 2008]. In the Mawrth Valles region, coordinated targeted observations reveal vertical layering of phyllosilicate composition consistent over hundreds of thousands of square kilometers [Bishop *et al.*, 2008; McKeown *et al.*, 2009]. A number of highland craters exhibit concentrations of phyllosilicate in the lower beds of fans interpreted as deltaic deposits formed in former intracrater lakes; these deposits are exobiologically important, because they may be capable of preserving organic chemistry formed in a habitable environment [Ehlmann *et al.*, 2008a]. In other topographically low areas in the highland plateau plains, phyllosilicates have been found to underlie previously recognized deposits interpreted to contain a large fraction of chloride minerals [Osterloo *et al.*, 2008]. Active investigation now centers on the depth, lateral extent, and continuity of phyllosilicates in the highlands [Murchie *et al.*, 2009a]. Two new classes of aqueous minerals have been detected from orbit in bedrock exposures, Noachian-aged carbonates [Ehlmann *et al.*, 2008b] and Hesperian-aged or younger hydrated silica [Milliken *et al.*, 2008]. The presence of carbonates demonstrates that at least parts of the Noachian crust escaped subsequent acidic conditions, and the carbonates' restricted extent places limits the amount of CO₂ from an ancient dense atmosphere that is trapped in crustal rocks. The presence of hydrated silica indicates that liquid water persisted later into Martian history than previous evidence had suggested.

[18] CRISM's higher spatial resolution coverage of sulfate-containing layered deposits also provides new constraints on the emplacement and distribution of those deposits. At various locations in and surrounding Valles Marineris, including Juventae Chasma [Bishop *et al.*, 2009], Candor Chasma [Murchie *et al.*, 2009b; Roach *et al.*, 2009], and Aram Chaos (K. Lichtenberg *et al.*, Stratigraphy of hydrated sulfates in the sedimentary deposits of Aram Chaos, Mars, submitted to *Journal of Geophysical Research*, 2009), layers containing monohydrated and polyhydrated sulfates form sharp contacts, and monohydrated sulfate usually underlies polyhydrated sulfate; in eastern Candor Chasma, they form a complex interbedded sequence. In Aram Chaos, the hydrated sulfates are in turn superposed on a thin layer of material containing a hydroxylated sulfate. The layering of sulfate mineralogies suggests either changes in the depositional environment or diagenesis [Murchie *et al.*, 2009b; Roach *et al.*, 2009]. Outlying occurrences of sulfate-containing layered material resembling the deposits in Meridiani Planum have been found to the east in Schiaparelli Crater [Wiseman *et al.*, 2009]. Sulfates have also been detected in layered, intracrater deposits in Terra Sirenum, where alunite and other sulfates occur together with the phyllosilicate mineral kaolinite [Swayze *et al.*, 2008; Wray *et al.*, 2008, 2009]; these deposits are interpreted as having formed in lacustrine environments. Overall, the spatial distribution of sulfate-bearing deposits is consistent with models of evaporite deposition by Hesperian-aged groundwater discharge, providing a unifying mechanism for emplacing these widely separated materials [Andrews-Hanna *et al.*, 2007; Murchie *et al.*, 2009b; Lichtenberg *et al.*, submitted manuscript, 2009].

[19] Finally, CRISM has also provided new evidence for geologically recent climate and present-day seasonal and

atmospheric phenomena. Late summer residuals of the seasonal polar cap correlate with high concentrations of hydrogen interpreted as ground ice, measured by the Mars Odyssey gamma-ray spectrometer [Calvin *et al.*, 2009]. This finding suggests a relationship between surficial occurrences of ice and either the present-day deposition of ground ice or the preservation of relict ground ice. During sublimation of CO₂ ice in the seasonal polar caps, the formation of fan- and spider-like features can be modeled by adiabatic cooling of CO₂ gas formed by solar heating under the ice that is released and freezes to form downwind frost streaks [Titus *et al.*, 2008]. Analysis of EPF measurements acquired during the "2007 global dust event" reveals that atmospheric dust has a higher single scattering albedo than previously assumed, providing up to 10°K less atmospheric heating (depending on altitude) than current global circulation models assume [Wolff *et al.*, 2009]. Spatial and seasonal variations in atmospheric gases, determined using the collection of EPF and TOD measurements, show that following the global dust event atmospheric H₂O vapor was unusually low compared with previous Mars years. For the first time, mapping of CO revealed spatial seasonal variations in column abundance where this gas was concentrated by autumn condensation of CO₂ in the seasonal polar caps, and diluted by its springtime sublimation [Smith *et al.*, 2009].

4. Data Product Generation

[20] The processing of CRISM data into data products delivered to the Planetary Data System (PDS) is shown schematically in Figure 4. Data products in PDS-compliant formats are generated in near real time and delivered every three months. Two types of products are delivered, "standard products" produced for all observations, and "special products" generated on a best effort basis.

4.1. Radiometric and Geometric Calibration

[21] Mars scene images are calibrated to I/F (the ratio of measured radiance to the incoming solar flux) in eight major steps, using the accompanying and interleaved instrument calibrations as well as ground-based calibrations. More detail is provided by Murchie *et al.* [2007a, 2007b]. In each case, scene data are processed using internal calibrations having the same frame rate that are taken close in time to a measurement covering a scene on Mars.

[22] 1. The component of the raw data numbers (DNs) due to counted photons is isolated and is corrected for the slightly nonlinear response of the detectors. To do this, for the IR detector, the DN levels are extracted from measurements taken during daily bias calibrations at multiple exposure times. For each detector element the measurements are fit linearly and the zero exposure-time intercept is taken as the bias, or response of the detector to zero photon inputs. The bias estimate is subtracted from shutter-closed background measurements, sphere measurements, and scene measurements. In each case the result is divided by the nonlinear response of the detector as a function of DN that was measured on ground. The result is a value in units of corrected DN that is proportional to counted photons. For the VNIR detector, the operating temperature is sufficiently low that shutter-closed background measure-

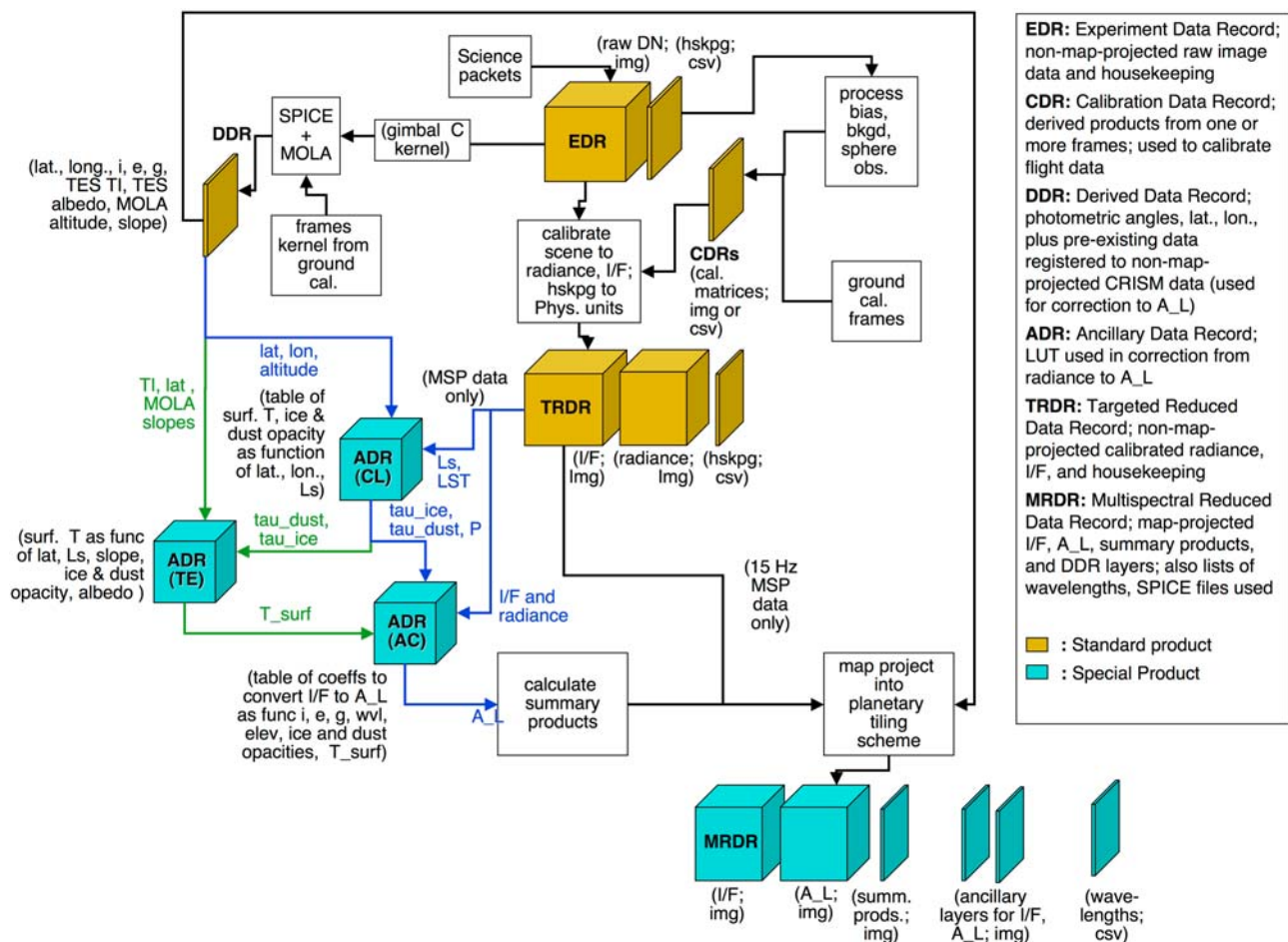


Figure 4. Schematic representation of pipeline processing of CRISM data products delivered to the Planetary Data System.

ments sample only bias without measurable dark current, so the background measurements are used instead of dedicated bias calibrations to estimate bias.

[23] 2. For the IR detector only, bias-corrected and linearized DN's from interleaved background measurements are subtracted from similarly corrected scene and integrating sphere measurements. This step removes internal emissions of the spectrometer cavity that illuminate the IR detector.

[24] 3. For both detectors, bias-, linearity-, and background-corrected scene and sphere data are divided by exposure time, yielding a result that is proportional to measured radiance.

[25] 4. For both detectors, at each row, the scattered light from the grating that is measured in dedicated columns at the edge of the scene and sphere images is subtracted from the data.

[26] 5. For both detectors, sphere measurements are divided by a ground-based model of the sphere's spectral radiance, yielding a measure of responsivity of each detector element. That responsivity is time-variable, and affected by detector temperature and temperature-dependent transmissivities of the beam splitter and of the detector-mounted filters. However, at VNIR wavelengths <560 nm the transmissive optics are spectrally featureless and the integrating

sphere has low spectral radiance, so a ground-based measurement of responsivity is used instead.

[27] 6. The processed scene data are divided by the responsivity model, yielding estimated scene spectral radiance.

[28] 7. Residual calibration nonuniformity is removed using a "flat field" correction. Scene measurements are in principle flat fielded using the radiometric model of the onboard integrating sphere, but there are artifacts in that model at the scale of one to several detector elements. To remove these, a flat field image was constructed from multiple measurements of bland, dusty regions of Mars, whose radiances were normalized to unity at each wavelength. The radiances of other scenes are divided by the flat field to correct the propagated artifacts.

[29] 8. Flat field-corrected scene radiances are divided by a solar spectrum convolved through CRISM's band passes measured on ground, scaled to Mars' solar distance, yielding I/F.

[30] Pointing calculations and geolocation are done on a pixel-by-pixel basis. Latitude and longitude are calculated for each pixel using the line of sight intercept of the field of view with the MOLA shape model of Mars. Photometric angles are evaluated relative both to the shape model and relative to the MOLA areoid. Ancillary data useful for further processing steps, including MOLA slope and slope

azimuth and TES bolometric albedo and thermal inertia, are resampled from publicly released data sets into the non map-projected sensor space of each detector element in the radiance and I/F data.

[31] The results of these steps are four complementary data sets containing raw data and the calibration files needed to process them, as well as data calibrated using the best algorithms available at the time of processing:

[32] 1. Experiment data records (EDRs) contain raw images taken either as scene measurements or during internal calibrations.

[33] 2. Targeted reduced data records (TRDRs) contain image data for all types of scene observations, calibrated to units of radiance and I/F.

[34] 3. Derived data records (DDR) contain image planes with the latitude, longitude, photometric angles, and other information for each image pixel in the TRDRs. The latitude and longitude support map projection of the TRDRs, whereas the photometric angles and ancillary information support correction of the TRDRs for illumination and atmospheric effects.

[35] 4. Calibration data records (CDRs) contain the vectors and matrices used to process data from raw form, including those derived from in-flight calibrations as well as ground-derived values. The calibration process is obviously complicated and users are not recommended to attempt to redo processing to the TRDR level themselves; rather, this is for archival purposes to assist in diagnosing artifacts in the calibrated data.

4.2. Additional Radiometric Corrections

[36] The most basic step in further processing of data calibrated to I/F is a correction for illumination effects and for attenuation by atmospheric gases. Three methods have been developed for this purpose. The first method, the “volcano scan correction,” is the correction typically applied to single targeted observations. The data are divided by the cosine of the solar incidence angle and by a scaled atmospheric transmission spectrum obtained during an observation crossing Olympus Mons [Bibring *et al.*, 2005; Mustard *et al.*, 2008]. This corrects for atmospheric gases but not aerosols. All of the information required for this operation is included with the data set delivered to the PDS. I/F comes directly from TRDRs, and solar incidence angles from the DDRs. The scaled atmospheric transmission spectrum and an explanation of its application are included as files formatted as CDRs, whose nomenclature begins with the string “CDR4_AT.” There are separate versions for each instrument configuration, as explained in documentation accompanying the delivered data. (A similar set of files containing the wavelengths for each detector element, used in spectral data analysis, has a nomenclature that begins with the string “CDR4_WA.”)

[37] The second atmospheric/photometric correction method, the “Lambert albedo correction,” is applied during standard processing to mosaics of multispectral data acquired over a range of atmospheric and illumination conditions. That method is discussed in more detail in section 4.4. The third method is applied to selected targeted observations. Using atmospheric gas and aerosol abundance from similar Ls as discussed in section 4.4 as a starting guess, the program Discrete Ordinates Radiative Transfer

(DISORT) [Stamnes *et al.*, 1988] is run iteratively to model both surface and atmospheric radiances to minimize atmospheric gas bands, and Lambert albedo is retrieved.

4.3. Data Accuracy and Precision

4.3.1. Radiometric Calibration Accuracy, Version History, and Caveats

[38] The goals for radiometric calibration accuracy developed for CRISM prior to MRO launch were (1) 10% absolute accuracy at 630 nm (to support mixture modeling using laboratory spectra); (2) 1% relative accuracy, comparing 0.45 and 0.75 μm (to measure the decrease in reflectance below 0.8 μm due to ferric iron); (3) 0.5% relative accuracy, for adjacent channels near 1 μm (to measure the 1- μm absorption due to ferrous and ferric minerals); (4) 0.25% relative accuracy, for adjacent channels near 2.3 μm (to measure absorptions due to phyllosilicates, hydrated silica and sulfates, and carbonates); and (5) 1% relative accuracy, comparing 1.6 μm versus 2.5 μm and 2.5 versus 3.1 μm (to measure spectral continuum, pyroxene absorption bands, and depth of the 3- μm H₂O absorption).

[39] Attainment of these goals was evaluated over the VNIR wavelength range by comparing CRISM data with simultaneously acquired PANCAM measurements of large, uniform areas at the MER landing sites (e.g., “Cliff Hanger” in Figure 19 of Arvidson *et al.* [2008]). Over the IR wavelength range it was evaluated by comparison of CRISM data with OMEGA measurements of the same sites. In both cases, corrections for photometric and atmospheric effects were made to simulate OMEGA or PANCAM data at CRISM geometry. The results of these comparisons and other results led to updates in the calibration; the values reported below pertain to the current version, version 2. In the comparison of CRISM’s VNIR wavelength range with PANCAM data, goal 1 (absolute calibration) is met, and goal 2 (spectral slope at 0.45–0.75 μm) is close to being met. The comparison of CRISM’s VNIR wavelength range at 440–1000 nm with PANCAM data suggests that absolute calibration at those wavelengths may be good typically to $\pm 5\%$. Independent comparison of CRISM’s VNIR wavelength range with MARCI data yields similar agreement to within ± 2 –3% [Wolff *et al.*, 2009]. The relative accuracy of wavelengths near 1 μm does not meet goal 3 and is closer to 1%, but is expected to meet this goal after the upgrade to calibration version 3 described below. Systematic channel-to-channel variations appear in multiple scenes and may be attributable to errors in the radiometric model of the integrating sphere; reduction of these artifacts is planned for version 3. The relative accuracy channel-to-channel near 2.3 μm either meets or is close to goal 4, 0.25%. Goal 5 was not initially met owing to errors in continuum slope as described below, that were addressed using CRISM observations of Deimos, but this goal may now be met.

[40] As is typical of other imaging investigations on planetary missions, as data were acquired in-flight, previously recognized calibration issues have become better quantified and some new issues have emerged. In response, the calibration algorithm goes through periodic upgrades. Which calibration version was used to process a particular observation is coded as the last character of the root file name. In addition, the full list of calibration files applied to the data is given in the detached PDS label. The initial

version of the calibration, version 0, was based on strict application of ground-derived performance (most notably the radiometric model of the integrating sphere), and using a relative simple estimate of scattered light from the grating (interpolating between values from the scattered light columns of the detector). Once Mars observations were acquired, several problems became apparent, especially (1) a field angle–dependent shape to VNIR spectra that was traced to the overly simplistic treatment of scattered light from the grating; (2) systematic, column-to-column differences in spectral shape, traced to uncorrected artifacts of noise in ground calibration data; (3) inaccurate spectral shape at VNIR wavelengths $<0.5\ \mu\text{m}$, traced to random noise and systematic processing errors using the low internal integrating sphere radiance at those wavelengths; (4) spurious, sharp peaks or troughs at boundaries of detector zones, traced to light leakage at the boundaries of the order-sorting filters; (5) shallow, systematic bumps at wavelengths where effects of atmospheric H_2O vapor were inaccurately removed from ground calibration data; (6) intermittently elevated values of I/F at particular detector columns and wavelengths, traced to uncorrected, transient elevated bias in particular detector elements, discussed below; and (7) a broad, shallow rise in I/F centered near $3.4\ \mu\text{m}$, resulting from incomplete implementation of a correction for leaked second-order light in zone 3 of the IR detector.

[41] The next version of the calibration, IR version 1 and VNIR version 2 (VNIR version 1 having been abandoned), addressed the first six of the above issues. Changes made to the processing included improved noise correction and interpolation across detector-zone boundaries in ground-based calibration data, modeling scattered light as a polynomial function of field angle, adoption of fixed values of responsivity at $<0.56\ \mu\text{m}$, and introduction of a rudimentary filter to interpolate over detector elements when they exhibit transient high bias levels.

[42] VNIR version 2 and IR version 1 were used in the comparison with OMEGA measurements of bland, dusty areas of Mars, and a comparison of CRISM measurements of Deimos with ground-based measurements [Lynch *et al.*, 2007]. Discrepancies drove an update in IR calibration to version 2. The comparison with OMEGA indicated systematic differences between the two data sets in continuum slope at $>1.5\ \mu\text{m}$ as well as a recurring, systematic “bump” near $2.55\ \mu\text{m}$. The same features appeared in the spectrum of Deimos, which is an ideal calibration target because its spectrum is believed to be smooth and it exhibits no atmospheric gas absorptions. The $2.55\text{-}\mu\text{m}$ bump was traced to incomplete removal of atmospheric water vapor from the spectra of the ground calibration standard used for the integrating sphere; the error in the continuum slope at $>1.5\ \mu\text{m}$ was modeled as a small pointing error at the ground calibration standard, which slightly vignettted the standard (incoming rays from the standard did not reach part of the aperture, affecting how the multizoned gratings were sampled). Corrections for both effects were derived from first principles of instrument performance. Additional changes in IR version 2 included (1) refinements to the corrections for noise and light leakage in detector-zone boundaries in ground-based calibration data; (2) increasing the threshold for filtering pixels with elevated bias, to remediate aliasing that the initial filter introduced into the

data; and (3) implementation of the correction for leaked second-order light in zone 3 of the IR detector. After all these changes, a shallow “ramp” remained near $1.9\ \mu\text{m}$ and it was corrected empirically.

[43] Six known issues remaining in VNIR and IR version 2 are being investigated, and will be addressed in an upgrade to “version 3” or later versions. The first issue is systematic channel-to-channel variations, discussed above, with will be addressed by removing the corresponding systematic error in the integrating sphere model. The second issue is the temporal drift in wavelength calibration, that is, the mapping of detector rows to wavelengths. Seasonal variations in optics temperatures introduced a time-dependent variation in CRISM’s wavelength calibration about 1 nm in magnitude (0.15 detector rows) [Smith *et al.*, 2009]. The inaccuracy in wavelength calibration results in errors in removal of CO_2 gas absorptions and elevation-dependent errors in the $2\text{-}\mu\text{m}$ wavelength region in atmospherically corrected data. The resulting artifact introduces error into 1.9- to $2.1\text{-}\mu\text{m}$ absorptions owing to ices and bound water. A time-dependent wavelength calibration has subsequently been developed that has with an accuracy of about 0.13 nm, as has a time-segmented volcano-scan atmospheric correction. Either the usage of the time-segmented volcano-scan correction or the incorporation of a time-dependent wavelength calibration into the Lambert albedo correction largely removes this effect. The third issue is high time-frequency variations in detector bias, or “noisy pixels,” which affect up to a couple percent of the IR detector elements. In spatial images at some wavelength, this appears as streaks, and the effect is worse and affects more detector elements at higher detector temperatures. The effects of these bias variations are being addressed using a kernel filter that identifies outlying values from various detector elements statistically, and then interpolates over them from the surrounding data. The fourth issue is a spurious peak or trough near $3.18\ \mu\text{m}$ that appears in parts of the field of view, intermittently. It has been traced to an artifact of the zone 1-zone 2 boundary in the correction for leaked second-order light in zone 3 of the IR detector, and is corrected in version 3. The fifth issue is time variations in spectral shape at $<1.5\ \mu\text{m}$ which result from slight irreproducibility in shutter position viewing the internal integrating sphere, that change the way integrating sphere radiance is sampled by the two zones of the IR grating. This is being corrected using the known effect of the phenomenon, which can be scaled from observation to observation by its signature at the boundary of the two VNIR detector zones. This may be remedied by shifting the wavelength of the correction. The final issue is high spectral frequency oscillations at >3300 . These are due to a Fabry-Perot effect in the zone of the detector-mounted filter that blocks out-of-order light at $>2.7\ \mu\text{m}$. Small variations in that filter’s temperature (thickness) between observations of Mars and of the internal integrating sphere cause $\sim 5\%$ oscillations in system response as a function of wavelength not to cancel out. This will be addressed by using weighted averages of temporally adjacent integrating sphere measurements, instead of using the closest one in time as is the current practice.

[44] Two other radiometric calibration issues are so integral to the data that further corrections are not likely. The first of these latter issues is incomplete removal of grating

scatter at $<0.44 \mu\text{m}$. At these wavelengths, for most Mars scenes, radiance is low and strongly affected by residuals from the correction for grating scatter. The second issue is leakage of light through boundaries of different zones of the detector-mounted filters. This leakage is scene-dependent and presently cannot be accurately estimated and removed.

[45] Given the various issues outlined above, some guidelines can be prescribed for reliability of the radiometric calibration at different wavelengths. The following channels at the ends of detector zones can be routinely excluded: (1) VNIR wavelengths less than 410 nm, between 644 and 684 nm, and greater than 1023 nm. (2) IR wavelengths less than 1021 nm, 2694 and 2701 nm, and greater than 3924 nm.

[46] The following channels may be degraded in their accuracy in some observations, but intrascene variations appear to be valid. In other words, information from the following channels can be recovered by ratioing to some spectrally bland part of the same scene, preferably in the same column(s) of an image: (1) VNIR wavelengths 410–442 nm (due to artifacts from the correction for grating scatter, in very contrasty scenes). (2) VNIR wavelengths 970–1023 nm and IR wavelengths 1021–1047 nm (the radiances can misalign between detectors; the reason is speculated to be uncorrected effects of beam splitter temperature). (3) IR wavelengths near 1650 nm surrounding the zone 1-zone 2 boundary. (4) IR wavelengths 2660–2800 nm (the reason is uncertain but may be due to problems with correction of water vapor in measurements of the ground calibration standard). (5) IR wavelengths greater than 3700 nm (there is a scene-dependent turn-down in radiances beyond 3700 nm due to unknown causes).

[47] In terms of scientific interpretation of the data, the implications of calibration artifacts depend on preprocessing and the scene. Where it is possible to ratio a region of interest to a spectrally bland region in or near the same detector column, narrow absorptions due to phyllosilicates, carbonates, silica, or sulfates can be measured in the relative spectra to an accuracy typically of much better than 1%. The information lost in the ratioing process is the visible wavelength red slope and the exact shape of the $1\text{-}\mu\text{m}$ absorption due to ferrous minerals. In unratiod spectra, the primary cautions on interpretations are that (1) uncorrected temporal variations in shape of IR spectra at $<1.5 \mu\text{m}$ can lead to errors in models of the relative abundances of olivine and pyroxene; (2) the $3.18\text{-}\mu\text{m}$ artifact can obscure the $3.4\text{-}\mu\text{m}$ carbonate absorption, where carbonate is present; and (3) errors in correction for atmospheric CO_2 at times of extreme instrument temperatures lead to a superimposed “ripple” near $2 \mu\text{m}$ that can partially obscure the $1.9\text{-}\mu\text{m}$ absorption owing to molecular H_2O -bearing phases.

4.3.2. Geometric Calibration

[48] The goal for accuracy in projection of CRISM data onto the MOLA shape model was 600 m. That goal was derived from an error estimate including expected knowledge of gimbal pointing, spacecraft position and attitude, and Mars cartographic control. In practice overlapping images have typically mosaicked with errors of 200 m or less indicating superior performance of all aspects of MRO and CRISM pointing.

4.4. Assembly of Map-Projected Multispectral Data

[49] Data taken as part of the multispectral survey are delivered to the PDS processed beyond the TRDR level, by applying an estimated correction for atmospheric and photometric effects, mosaicking the image strips, and calculating spectral parameters that give an overview of the data content. The assembled map is divided into 1964 separate tiles, each covering 5° in latitude with an approximately square outline.

4.4.1. Correction for Atmospheric and Photometric Effects

[50] The procedure for correcting multispectral survey measurements is described in detail by McGuire *et al.* [2008]. The correction is done using three external, pregenerated, hyperdimensional lookup tables. Using the latitude, longitude, elevation, L_s , and local solar time for a pixel extracted from the appropriate DDR, the column abundances of atmospheric gases and aerosols are retrieved from a “climatology” lookup table (“ADR_CL”) that represents average conditions from previous Mars years measured by TES. Next for the latitude, L_s , surface slope azimuth and magnitude, and TES bolometric albedo and thermal inertia retrieved from the DDR and the dust and ice aerosol opacities retrieved from the ADR_CL, surface-temperature for the pixel is retrieved from another lookup table (“ADR_TE”). Finally, for an I/F at some wavelength from the scene data, and values retrieved from the corresponding pixel location in the DDR and from the ADRs, a multiplicative correction that was precomputed using DISORT [Stamnes *et al.*, 1988] is retrieved from a third lookup table (“ADR_AC”) and applied. The output, “Lambert albedo,” is an estimate of the surface I/F for hypothetical normal illumination and viewing geometry in the absence of an atmosphere and thermal emission.

[51] Both the Lambert albedo and volcano-scan corrections have limitations that affect interpretability of the data especially at $<0.8 \mu\text{m}$ and near $2 \mu\text{m}$. Both methods are affected by a time-dependent drift of approximately $\pm 1 \text{ nm}$ in wavelength calibration, as was described in section 4.3.1. This shift introduces artifacts from inaccurate modeling and removal of the $2\text{-}\mu\text{m}$ CO_2 absorption. In addition, the volcano scan correction does not explicitly correct for scattering effects of atmospheric aerosols, leading to higher-than-actual values of corrected I/F at most wavelengths. In contrast, the Lambert albedo correction does explicitly correct for aerosols, using a model for dust scattering and climatological predictions of aerosol optical depth. The effects of this approach are concentrated at shorter wavelengths, but extend to all wavelengths in specific seasons as discussed at greater length in section 4.4.3. Finally, both corrections assume Lambertian scattering from the surface, instead of using more accurate Hapke scattering functions [e.g., Johnson *et al.*, 2006], introducing systematic errors to corrected I/F that depend on the photometric geometry of the observation.

4.4.2. Calculation of Summary Products

[52] Summary products are described by Pelkey *et al.* [2007] and represent spectral indices indicative of the occurrence of different mineral phases and atmospheric constituents. Summary products may also be affected by dependencies on solar incidence angle, surface slopes, atmospheric conditions, detector artifacts, and response to

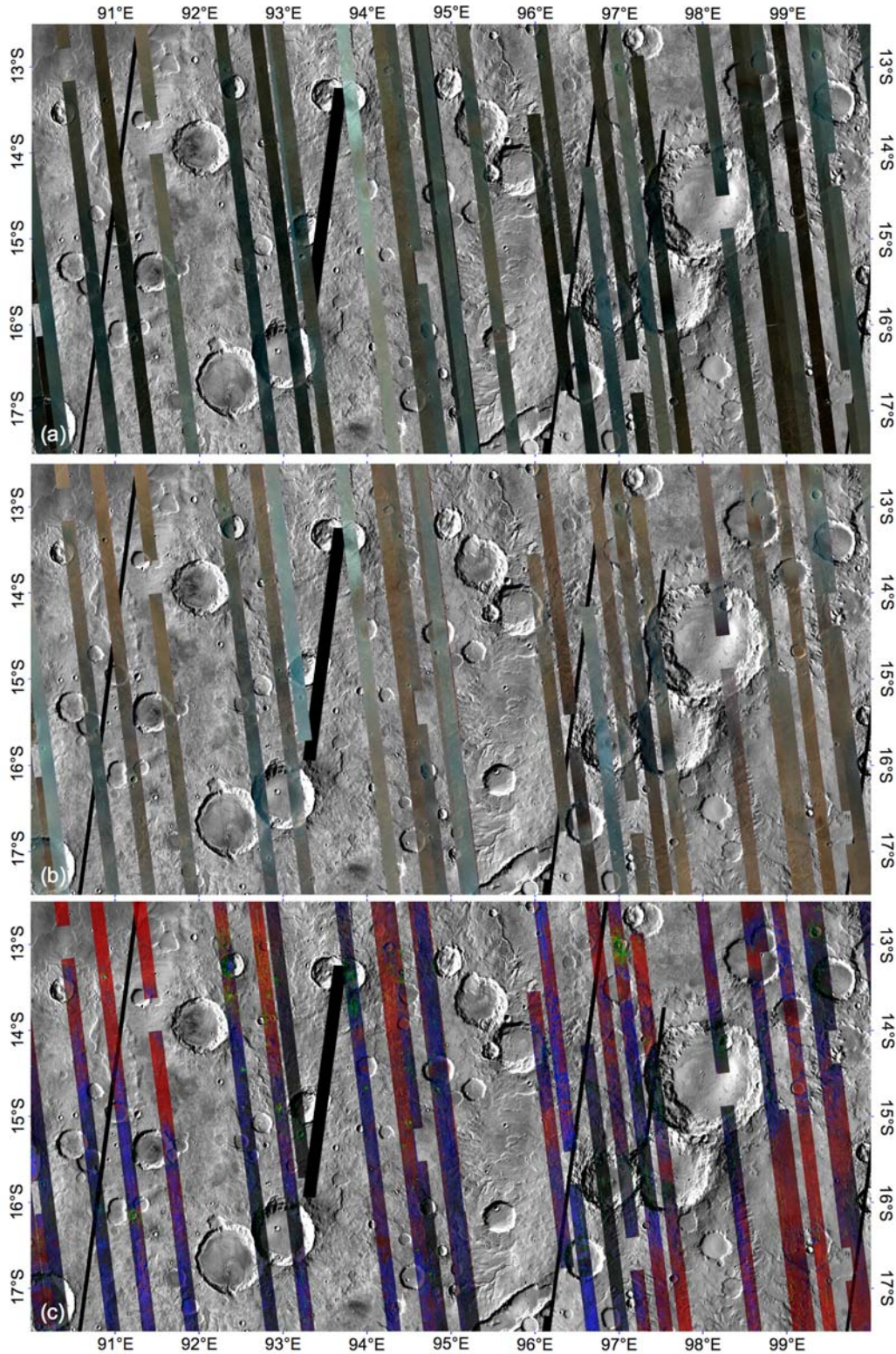


Figure 5. Examples of the three versions of map-projected multispectral survey data that are delivered to the Planetary Data System, shown overlain on a Thermal Emission Imaging System day-IR mosaic. The two tiles shown, 750 and 751, cover part of Tyrrhena Terra. (a) I/F, with 2.53-, 1.50-, and 1.08- μm wavelengths shown in the red, green, and blue image planes. (b) Same as in Figure 5a except that the data have been corrected to Lambert albedo. (c) Summary products with OLINDEX (a measure of the strength of the 1- μm absorption due to olivine or dust) shown in the red image plane, D2300 (a measure of the 2.3- μm absorption due to Fe/Mg-phyllosilicates) in the green image plane, and HCPINDEX (a measure of the strengths of 1- and 2- μm absorptions due to pyroxene) in the blue image plane.

phases other than what the products were intended to show. Still, the summary products are useful as a guide indicating regions of possible mineralogic interest where further spectral analysis may be conducted to positively identify mineral phases.

[53] Currently, 45 summary products are routinely calculated from CRISM data and are described by *Murchie et al.* [2007b]. Two are Lambert albedos at reference wavelengths. Thirty-two, which are calculated from Lambert albedo, represent spectral ratios or band depths possibly indicative of absorptions due to H₂O and CO₂ ices, Fe minerals, sulfates, phyllosilicates, or additional phases such as carbonates. Eleven more, calculated from I/F without additional corrections, represent spectral ratios or band depths indicative of atmospheric aerosols or trace gases. Most of the summary products are based on variations that occupy a few percent or less of the dynamic range at their wavelengths, respectively, so noise reduction filtering is applied to lessen the effects of systematic instrument artifacts that escape correction during calibration.

[54] The summary products serve as “indicators” sensitive to the presence of specific classes of mineral phases, and as such cannot be treated as relative abundance maps or even definitive detections. Strength of the absorptions coded in the summary products can be modulated by particle size, coverage by dust, and obscuration by atmospheric dust and ice aerosols as well as by abundance of the phase of interest. Furthermore, parameters designed to respond to some mineral classes can also respond to others; for example, the parameter designed to detect a 1.9- μ m absorption due to bound molecular water also responds to the 2- μ m absorption in H₂O ice and to the broad, shallow 2- μ m absorption due to pyroxene. Thus, summary parameters should be treated as indicators of where (spatially) to apply further analyses to the underlying spectral data.

4.4.3. Construction of Map Tiles

[55] To create a more user-friendly, systematic product, the data are organized into 1964 separate tiles (Multispectral Reduced Data Records, or MRDRs) that sample the planet’s surface at 256 pixels per degree. The resulting map pixel size of 231 m is well matched to the native resolution of the multispectral survey, and the tiles provide a convenient approach to managing the extremely large data volume (2.6 TB) of the whole map. The full map consists of five parallel data product sets: I/F, Lambert albedo, summary products, and ancillary data for both the I/F and Lambert albedo tiles. The ancillary information provides traceability to source observations (observation number, line and sample in the source product) and their conditions (e.g., photometric geometries and solar longitude). Images are map-projected using nearest-neighbor resampling to preserve values in the original data. The order of stacking is with minimum incidence angle on top, to maximize the area covered at favorable illumination and with a minimum of frost or ice cover. To exclude images obscured by the global dust event of 2007, only observations acquired prior to 25 June 2007 and after 29 September 2007 are used to build MRDRs.

[56] Figure 5 provides an example of the contents of the map tiles, using two tiles (750 and 751) that cover part of Tyrrhena Terra. The I/F version of the tiles (Figure 5a) retains all of the spectral and spatial variations owing to

illumination and atmospheric conditions as well as geologic materials on the surface. It provides a useful starting point for alternative corrections to those applied in the data processing pipeline, and its accompanying ancillary data support those corrections. Mapped Lambert albedo (Figure 5b) exhibits improved continuity between nearby strips of multispectral survey data. However, some individual strips mismatch their neighbors where atmospheric conditions significantly departed from past climatology, and where high solar incidence angles yielded poor corrections. In addition Lambert albedos at <800 nm are spuriously low. This is attributable to the palagonite-based scattering model for atmospheric dust used in the precomputed corrections. It was found to differ significantly from scattering properties actually measured by CRISM during the 2007 global dust event [Wolff *et al.*, 2007]. The mapped summary products (Figure 5c) exhibit good cross-track continuity except in strips where the actual atmospheric conditions departed from climatologic averages. Summary products showing mineralogic absorptions at <0.8 μ m are inaccurate owing to poor corrections for atmospheric dust, and those showing mineralogic absorptions near 2.0 μ m exhibit weak artifacts of elevation owing to errors in modeling and removing atmospheric CO₂. In the part of Mars shown in Figure 5, most spectral variations are related to differences in the relative strengths of absorptions owing to olivine and high-calcium pyroxene. Fe/Mg-phyllosilicates are exposed in crater walls, rims, and ejecta.

5. Plans for the Extended Science Phase

[57] CRISM’s investigation during the ESP will build on results from the PSP. Five major goals for targeted observations are to (1) sample thousands more outcrops identified in the multispectral survey that probe the structure of the Noachian crust and the distribution of aqueous minerals; (2) map the lateral variations in crustal layering exposed in the walls of Valles Marineris; (3) densely sample geologically complicated aqueous deposits (e.g., in Valles Marineris, Mawrth Valles, and Nili Fossae); (4) monitor interannual variations in condensation and sublimation of seasonal polar ices; and (5) image targets to support selection and characterization of future landing sites.

[58] Typically, observations will be coordinated with HiRISE and CTX. CRISM will also continue building up multispectral and atmospheric survey observations with the objectives of (1) filling gaps in the multispectral survey and (2) continued monitoring of the atmosphere using EPF grids and TODs.

[59] Deliveries of standard data products to the PDS will continue as during the PSP, and two major classes of new special products are being developed for release. The first new class of products is a second generation of MRDRs to reduce known data artifacts. The time-dependent wavelength calibration will be incorporated into the correction of multispectral data to Lambert albedo. This update will minimize or remove the 2- μ m artifact from inaccurate removal of the atmospheric CO₂ absorption. THEMIS, CRISM and MARCI data are being used to develop an updated version of the climatology lookup table (“ADR_CL”) that represents actual atmospheric conditions during the PSP, rather than a prediction based

on climatology. This update will minimize the mismatch of overlapping MSP strips acquired at different times. Finally, scattering properties of atmospheric dust are being updated using results from CRISM EPF measurements, and a second version of the lookup table to correct from I/F to Lambert albedo (“ADR_AC”) will yield improved accuracy at $<0.8 \mu\text{m}$.

[60] Second, an atmospherically corrected and map projected version of targeted observations is being developed for release. These new products will be generated using approaches similar to those used to create MRDRs, with three exceptions:

- [61] 1. Each map product will show only a single image.
- [62] 2. The map scale will be 3072 pixels per degree, yielding a map pixel 19.3 m in scale, which is well matched to the native resolution of targeted observation.
- [63] 3. A simplified atmospheric and photometric correction will be employed. Values of I/F are divided by cosine of the solar incidence angle, and corrected for atmospheric effects using the volcano scan correction. This approach corrects for atmospheric gases but not aerosols.

[64] **Acknowledgments.** The authors wish to thank all of the members of the CRISM and OMEGA teams who have contributed to planning and validation of CRISM observations and to testing of updates to the instrument calibration.

References

- Andrews-Hanna, J., R. Phillips, and M. Zuber (2007), Meridiani Planum and the global hydrology of Mars, *Nature*, **446**, 163–168, doi:10.1038/nature05594.
- Arvidson, R. E., et al. (2008), Spirit Mars Rover mission to the Columbia Hills, Gusev Crater: Mission overview and selected results from the Cumberland Ridge to Home Plate, *J. Geophys. Res.*, **113**, E12S33, doi:10.1029/2008JE003183.
- Bibring, J.-P., et al. (2005), Mars surface diversity as revealed by the OMEGA/Mars Express observations, *Science*, **307**, 1576–1581, doi:10.1126/science.1108806.
- Bibring, J.-P., et al. (2006), Global mineralogical and aqueous Mars history derived from OMEGA/Mars Express data, *Science*, **312**, 400–404, doi:10.1126/science.1122659.
- Bishop, J., E. Noe Dobrea, S. Murchie, C. Weitz, W. Calvin, L. Roach, S. Pelkey, A. Brown, J. Mustard, and J.-P. Bibring (2007), Sulfates and mafic minerals in Juventae Chasma as seen by CRISM in coordination with OMEGA, HiRISE and context images, in *Seventh International Conference on Mars*, July 9–13, 2007, Pasadena CA [CD-ROM], *LPI Contrib.*, **1353**, Abstract 3350.
- Bishop, J. L., et al. (2008), Phyllosilicate diversity and past aqueous activity revealed at Mawrth Vallis, Mars, *Science*, **321**, 830–833, doi:10.1126/science.1159699.
- Bishop, J. L., et al. (2009), Mineralogy of Juventae Chasma: Sulfates in the light-toned mounds, mafics in the sand, and opal in the plains, *J. Geophys. Res.*, doi:10.1029/2009JE003352, in press.
- Calvin, W., L. Roach, F. Seelos, K. Seelos, R. Green, S. Murchie, and J. Mustard (2009), CRISM observations of northern Martian latitudes in summer, *J. Geophys. Res.*, doi:10.1029/2009JE003348, in press.
- Christensen, P. R., R. V. Morris, M. D. Lane, J. L. Bandfield, and M. C. Malin (2001a), Global mapping of Martian hematite mineral deposits: Remnants of water-driven processes on early Mars, *J. Geophys. Res.*, **106**, 23,873–23,885, doi:10.1029/2000JE001415.
- Christensen, P. R., et al. (2001b), Mars Global Surveyor Thermal Emission Spectrometer experiment: Investigation description and surface science results, *J. Geophys. Res.*, **106**, 23,823–23,871, doi:10.1029/2000JE001370.
- Christensen, P. R., et al. (2004), The Thermal Emission Imaging System (THEMIS) for the Mars 2001 Odyssey Mission, *Space Sci. Rev.*, **110**, 85–130.
- Edwards, C. S., P. R. Christensen, and V. E. Hamilton (2008), Evidence for extensive olivine-rich basalt bedrock outcrops in Ganges and Eos chasmas, Mars, *J. Geophys. Res.*, **113**, E11003, doi:10.1029/2008JE003091.
- Ehlmann, B. L., J. F. Mustard, C. I. Fassett, S. C. Schon, J. W. Head III, D. J. DesMarais, J. A. Grant, and S. L. Murchie (2008a), Clay-bearing minerals and organic preservation potential in sediments from a Martian delta environment, Jezero crater, Nili Fossae, Mars, *Nat. Geosci.*, **1**, 355–358, doi:10.1038/ngeo207.
- Ehlmann, B., et al. (2008b), Orbital identification of carbonate-bearing rocks on Mars, *Science*, **322**, 1828–1832, doi:10.1126/science.1164759.
- Gendrin, A., et al. (2005), Sulfates in Martian layered terrains: The OMEGA/Mars Express view, *Science*, **307**, 1587–1591, doi:10.1126/science.1109087.
- Hamilton, V. E., and P. R. Christensen (2005), Evidence for extensive, olivine-rich bedrock on Mars, *Geology*, **33**, 433–436, doi:10.1130/G21258.1.
- Hoefen, T. M., R. N. Clark, J. L. Bandfield, M. D. Smith, J. C. Pearl, and P. R. Christensen (2003), Discovery of olivine in the Nili Fossae region of Mars, *Science*, **302**, 627–630, doi:10.1126/science.1089647.
- Johnson, J. R., et al. (2006), Spectrophotometric properties of materials observed by Pancam on the Mars Exploration Rovers: 2. Opportunity, *J. Geophys. Res.*, **111**, E12S16, doi:10.1029/2006JE002762.
- Langevin, Y., F. Poulet, J.-P. Bibring, and B. Gondet (2005), Sulfates in the north polar region of Mars detected by OMEGA/Mars Express, *Science*, **307**, 1584–1587, doi:10.1126/science.1109091.
- Lynch, D. K., R. W. Russell, R. J. Rudy, S. Mazuk, C. Venturini, H. B. Hammel, M. V. Sykes, R. C. Puetter, and R. B. Perry (2007), Infrared spectra of Deimos (1–13 μm) and Phobos (3–13 μm), *Astron. J.*, **134**, 1459–1463, doi:10.1086/519975.
- Malin, M. C., G. E. Danielson, A. P. Ingersoll, H. Masursky, J. Veverka, M. A. Ravine, and T. A. Soulanille (1992), The Mars Observer Camera, *J. Geophys. Res.*, **97**, 7699–7718, doi:10.1029/92JE00340.
- Malin, M. C., et al. (2007), Context Camera investigation on board the Mars Reconnaissance Orbiter, *J. Geophys. Res.*, **112**, E05S04, doi:10.1029/2006JE002808.
- McCleese, D. J., J. T. Schofield, F. W. Taylor, S. B. Calcutt, M. C. Foote, D. M. Kass, C. B. Leovy, D. A. Paige, P. L. Read, and R. W. Zurek (2007), Mars climate sounder: An investigation of thermal and water vapor structure, dust and condensate distributions in the atmosphere, and energy balance of the polar regions, *J. Geophys. Res.*, **112**, E05S06, doi:10.1029/2006JE002790.
- McEwen, A. S., et al. (2007), Mars Reconnaissance Orbiter's High Resolution Imaging Science Experiment (HiRISE), *J. Geophys. Res.*, **112**, E05S02, doi:10.1029/2005JE002605.
- McGuire, P. C., et al. (2008), CRISM retrieval of surface Lambert albedos for multispectral mapping of Mars with DISORT-based radiative transfer modeling, *IEEE Trans. Geosci. Remote Sens.*, **46**, 4020–4040, doi:10.1109/TGRS.2008.2000631.
- McKeown, N. K., J. L. Bishop, E. Z. Noe Dobrea, M. Parente, B. L. Ehlmann, J. F. Mustard, S. L. Murchie, J.-P. Bibring, and E. Silver (2009), Characterization of phyllosilicates observed in the central Mawrth Vallis region, Mars, their potential formational processes, and implications for past climate, *J. Geophys. Res.*, doi:10.1029/2008JE003301, in press.
- Milliken, R., et al. (2008), Opaline silica in young deposits on Mars, *Geology*, **36**, 847–850, doi:10.1130/G24967A.1.
- Murchie, S., et al. (2007a), Compact Reconnaissance Imaging Spectrometer for Mars (CRISM) on Mars Reconnaissance Orbiter (MRO), *J. Geophys. Res.*, **112**, E05S03, doi:10.1029/2006JE002682.
- Murchie, S., E. Guinness, and S. Slavney (2007b), CRISM data product software interface specification, http://pds-geosciences.wustl.edu/mro-crisp/mro-m-crisp-2-edr-v1/mrocr_0001/document/crisp_dpsis.pdf, NASA Planet. Data Syst., Greenbelt, Md., 17 Aug.
- Murchie, S. L., et al. (2009a), A synthesis of Martian aqueous mineralogy after 1 Mars year of observations from the Mars Reconnaissance Orbiter, *J. Geophys. Res.*, doi:10.1029/2009JE003342, in press.
- Murchie, S., et al. (2009b), Evidence for the origin of layered deposits in Candor Chasma, Mars, *J. Geophys. Res.*, doi:10.1029/2009JE003343, in press.
- Mustard, J., et al. (2008), Hydrated silicate minerals on Mars observed by the CRISM instrument on MRO, *Nature*, **454**, 305–309, doi:10.1038/nature07097.
- Osterloo, M. M., V. E. Hamilton, J. L. Bandfield, T. D. Glotch, A. M. Baldridge, P. R. Christensen, L. L. Tornabene, and F. S. Anderson (2008), Chloride-bearing materials in the southern highlands of Mars, *Science*, **319**, 1651–1654, doi:10.1126/science.1150690.
- Pelkey, S. M., et al. (2007), CRISM multispectral summary products: Parameterizing mineral diversity on Mars from reflectance, *J. Geophys. Res.*, **112**, E08S14, doi:10.1029/2006JE002831.
- Roach, L. H., J. F. Mustard, S. L. Murchie, J.-P. Bibring, F. Forget, K. W. Lewis, O. Aharonson, M. Vincendon, and J. L. Bishop (2009), Testing evidence of recent hydration state change in sulfates on Mars, *J. Geophys. Res.*, **114**, E00D02, doi:10.1029/2008JE003245.
- Seu, R., et al. (2007), SHARAD sounding radar on the Mars Reconnaissance Orbiter, *J. Geophys. Res.*, **112**, E05S05, doi:10.1029/2006JE002745.

- Smith, M. D., M. J. Wolff, R. T. Clancy, and S. L. Murchie (2009), Compact Reconnaissance Imaging Spectrometer observations of water vapor and carbon monoxide, *J. Geophys. Res.*, *114*, E00D03, doi:10.1029/2008JE003288.
- Stamnes, K., S.-C. Tsay, K. Jayaweera, and W. Wiscombe (1988), Numerically stable algorithm for discrete-ordinate-method radiative transfer in multiple scattering and emitting layered media, *Appl. Opt.*, *27*, 2502–2509, doi:10.1364/AO.27.002502.
- Swayze, G. A., et al. (2008), Discovery of the acid-sulfate mineral alunite in Terra Sirenum, Mars, using MRO CRISM: Possible evidence for acid-saline lacustrine deposits?, *Eos Trans. AGU*, *89*(53), Fall Meet. Suppl., Abstract P44A–04.
- Titus, T. N., T. I. Michaels, A. Colaprete, H. H. Kieffer, Y. Langevin, S. L. Murchie, and M. Vincendon (2008), Exotic processes within the cryptic region of Mars: A new method for near real-time estimates of wind direction, in *Third International Workshop on the Mars Atmosphere: Modeling and Observations, November 10–13, 2008, Williamsburg, VA, LPI. Contrib.*, *1447*, Abstract 9043.
- Wiseman, S. M., R. E. Arvidson, R. V. Morris, S. L. Murchie, F. P. Seelos, J. C. Andrews-Hanna, and CRISM Team (2009), Hydrated sulfate deposits detected within Schiaparelli Crater, Mars, *Lunar Planet. Sci.*, *XL*, Abstract 1798.
- Wolff, M., R. T. Clancy, M. D. Smith, R. E. Arvidson, B. Cantor, M. Kahre, R. Morris, and F. Seelos (2007), Investigating the wavelength dependence of the single scattering albedo of Martian dust aerosols with CRISM and MARCI observations of the very dusty atmosphere in 2007, *Eos Trans. AGU*, *88*(52), Fall Meet. Suppl., Abstract P31D–03.
- Wolff, M., M. Smith, R. T. Clancy, R. Arvidson, M. Kahre, F. Seelos IV, S. Murchie, and H. Savijarvi (2009), Wavelength dependence of dust aerosol single scattering albedo as observed by the Compact Reconnaissance Imaging Spectrometer, *J. Geophys. Res.*, *114*, E00D04, doi:10.1029/2009JE003350.
- Wray, J. J., et al. (2008), Clays and sulfates in a potential lacustrine evaporite sequence at Columbus Crater, Mars, *Eos Trans. AGU*, *89*(53), Fall Meet. Suppl., Abstract P53B–1446.
- Wray, J. J., S. L. Murchie, S. W. Squyres, F. P. Seelos, and L. L. Tornabene (2009), Diverse aqueous environments on ancient Mars revealed in the southern highlands, *Geology*, doi:10.1130/G30331A.1, in press.
- Zurek, R. W., and S. E. Smrekar (2007), An overview of the Mars Reconnaissance Orbiter (MRO) science mission, *J. Geophys. Res.*, *112*, E05S01, doi:10.1029/2006JE002701.

R. E. Arvidson and P. McGuire, Department of Earth and Planetary Sciences, Washington University, Saint Louis, MO 63130, USA.

O. S. Barnouin-Jha, D. L. Buczkowski, T. H. Choo, C. A. Harvel, D. C. Humm, J. A. McGovern, M. F. Morgan, S. L. Murchie, H. Nair, G. W. Patterson, F. P. Seelos, K. D. Seelos, and H. W. Taylor, Johns Hopkins University Applied Physics Laboratory, Laurel, MD 20723, USA.

J.-P. Bibring and F. Poulet, Institut d'Astrophysique Spatiale, Université Paris Sud, F-91405 Orsay, France.

C. D. Hash and E. Malaret, Applied Coherent Technology, 112 Elden Street, Herndon, VA 20170, USA.

J. F. Mustard, Department of Geological Sciences, Brown University, Providence, RI 02912, USA.

M. D. Smith, NASA Goddard Space Flight Center, 8800 Greenbelt Road, Greenbelt, MD 20771, USA.

T. N. Titus, U.S. Geological Survey, 2255 North Gemini Drive, Flagstaff, AZ 86001, USA.

M. J. Wolff, Space Science Institute, 4750 Walnut Street, Boulder, CO 80301, USA.